Title

Artificial Iron Proteins: Modeling the Active Sites in Non-Heme Dioxygenases

Journal

Inorganic Chemistry, 59(9)

ISSN

0020-1669

Authors

Miller, Kelsey R
Paretsky, Jonathan D
Follmer, Alec H
et al.

Publication Date

2020-05-04

DOI

10.1021/acs.inorgchem.9b03791

Peer reviewed

HHS Public Access

Author manuscript

Inorg Chem. Author manuscript; available in PMC 2020 July 04.

Published in final edited form as:

Inorg Chem. 2020 May 04; 59(9): 6000–6009. doi:10.1021/acs.inorgchem.9b03791.

Artificial Iron Proteins: Modeling the Active Sites in Non-Heme Dioxygenases

Kelsey R. Miller[†], **Jonathan D. Paretsky**[†], **Alec H. Follmer**[†], **Tillmann Heinisch**[‡,‖], **Kaustuv Mittra**[⊥], **Sheraz Gul**[¶], **In-Sik Kim**[¶], **Franklin D. Fuller**[#], **Alexander Batyuk**[#], **Kyle D. Sutherlin**[¶], **Aaron S. Brewster**, **Asmit Bhowmick**[¶], **Nicholas K. Sauter**[¶], **Jan Kern**[¶], **Junko Yano**[¶], **Michael T. Green**[†,⊥], **Thomas R. Ward**[‡], **A. S. Borovik**[†,*]

[†] Department of Chemistry, 1102 Natural Science II, University of California, Irvine, CA 9269 [⊥] Department of Molecular Biosciences and Biochemistry, University of California, Irvine, CA 92697 [‡] Department of Chemistry, University of Basel, PO Box 3350, Mattenstrasse 24a, BPR 1096, CH-4002 Basel, Switzerland [¶] Molecular Biophysics and Integrated Bioimaging Division, Lawrence Berkeley National Laboratory, Berkeley, California 94720, USA [#] Linac Coherent Light Source, SLAC National Accelerator Laboratory, Menlo Park, California 94025 USA

Abstract

An important class of non-heme dioxygenases contain a conserved Fe binding site that consists of a 2-His-1-carboxylate facial triad. Results from structural biology show that in the resting state, these proteins are six-coordinate with aqua ligands occupying the remaining three coordination sites. We have utilized biotin-streptavidin (Sav) technology to design new artificial Fe proteins (ArMs) that have many of the same structural features found within active sites of these non-heme dioxygenases. A Sav variant was isolated that contains the $S_{112}E$ mutation which installed a carboxylate side-chain in the appropriate position to bind to a synthetic Fe^{II} complex confined within Sav. Structural studies using X-ray diffraction (XRD) methods revealed a facial triad binding site that is composed of two N-donors from the biotinylated ligand and the monodentate coordination of the carboxylate from $S_{112}E$. Two aqua ligands complete the primary coordination sphere of the Fe^{II} center with both involved in hydrogen bond networks within Sav. The corresponding Fe^{III} protein was also prepared and structurally characterized to find a six-coordinate complex with two exogenous acetato ligands. The Fe^{III} protein was further shown to bind an exogenous azido ligand through replacement of one acetato ligand. Spectroscopic studies of the ArMs in solution support the results found by XRD.

[*]Corresponding Author aborovik@uci.edu.
[‖]Present Addresses DNAScript, Paris, France.

ASSOCIATED CONTENT

Supporting Information.

The Supporting Information is available free of charge on the ACS Publication website at DOI: The following file is available free of charge.

Details of X-ray diffraction, XFEL, and XAS data collections and processing, Figures S1-S8, Tables S1-S6, and Scheme 1 (PDF)

Accession Codes

PDB 6UIY, 6UIU, 6UIO, 6US6, 6UIZ contain the supplementary crystallographic data for this paper. These data can be obtained free of charge via https://www.rcsb.org/

The authors declare no competing financial interest.

Synopsis and Graphical Abstract

Biological O_2 activation is often accomplished with dioxygenases that contain non-heme iron centers with a common 2-His-1-carboxylate endogenous binding site for iron. We have engineered an artificial protein to model this site using biotin-streptavidin technology. Structural and spectroscopic studies support formation of an Fe(II) artificial protein with similar features as those in the native proteins, including hydrogen bonds within the secondary coordination sphere. This work highlights the utility of embedding metal complexes with protein hosts.

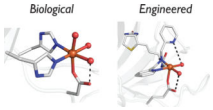

Keywords

Artificial Metalloproteins; Non-Heme Iron Proteins; Bioinorganic Chemistry

Introduction

Mononuclear non-heme Fe oxygenases are enzymes that catalyze a wide range of oxidative transformations using dioxygen as the terminal oxidant.[1–7] Many of these enzymes share a common Fe binding site that is composed of side chains from two histidine and either a glutamate or aspartate amino acid residues.[8–10] This endogenous binding site coordinates an Fe center in a facial manner and is referred to as the 2-His-1-carboxylate facial triad.[11] Information from structural biology indicates that in the FeII resting state of these proteins, and in the absence of any exogenous cofactors, the remaining coordination sites are occupied by water molecules (Figure 1).[12–14] A common feature of these structures is the presence of an intramolecular hydrogen bond (H-bond) between one of the aqua ligands and the carbonyl group of the coordinated carboxylate ligand.

Attempts to model this type of coordination environment include synthetic systems that catalyze the epoxidation and/or cis-dihydroxylation of olefins with H_2O_2 and O_2,[15,16] and the intramolecular arene hydroxylation of benzoylformate with O_2.[17–19] However, it has proven challenging to develop synthetic complexes whose coordination spheres resemble those found within these proteins. For instance, reported complexes that emulate the facial triad have been derived from sterically hindered N-donors and terphenylcarboxylate ligands[20] and tripodal ligands[21–30] but lack the aqua ligands found within protein active sites. In addition, these systems do not replicate the control over the secondary coordination spheres that is seen in metalloproteins.

We have utilized a complementary approach to develop bio-relevant Fe active sites that combine synthetic inorganic chemistry and protein engineering to design artificial metalloproteins (ArMs).[31–37] The approach capitalizes on biotin-streptavidin (Sav) technology to predictably insert biotinylated synthetic complexes into variants of Sav.[38–41] We reasoned that these protein hosts could provide ligands within the primary coordination sphere and simultaneously influence the secondary coordination sphere to better emulate natural active sites. Moreover, these constructs would be stable in aqueous solution allowing

for water to act as a ligand, as is found in natural metalloproteins. Our previous work has shown how the primary coordination sphere can be manipulated to produce ArMs that model the properties in cupredoxins through engineering an endogenous thiolate ligand into Sav that forms a strong covalent bond to the Cu centers.[42] Moreover, we have demonstrated that Sav can regulate the secondary coordination sphere around a Cu–hydroperoxido complex using intramolecular H-bonding networks.[43] In this report, we describe the design and development of new artificial Fe proteins that simulate the 2-His-1-carboxylate facial triad active site in non-heme monooxygenases. Both primary and secondary coordination spheres of the Fe centers are influenced by the Sav host to produce the new ArMs in which intramolecular H-bonds play a key structural role.

Results and Discussion

Design Concepts, Preparations, and Solution Properties of the Fe ArMs.

Previous work in our group found that binding of an endogenous ligand from Sav to a synthetic metallocofactor is possible. Our work on Type 1 Cu sites showed how Cu–$S_{thiolate}$ coordination could be achieved by using a relatively short ethylene linker between the biotin and synthetic complex that positioned the Cu center close to the residue at position 112.[42] We reasoned that Fe complexes prepared from the similar construct, bis(2-pyridylmethyl)amine (Figure 2: biot-et-dpa), may also place the metal center near this residue. Introduction of a $S_{112}E$ mutation in Sav would produce a variant that could then promote Fe–$O_{carboxylate}$ bond formation. In addition, the Sav host was re-engineered to incorporate two additional mutations, $K_{121}A/E_{101}Q$, as described previously.[44] The parent protein host is referred to as 2xm-Sav and the specific protein host used to develop mononuclear Fe sites is denoted 2xm-S_{112}E-Sav.

The biotinylated biot-et-dpa construct was prepared via a 3-step route from dpa (Scheme S1) using a modified literature procedure.[42] Formation of the Fe^{II} complex was achieved by treating biot-et-dpa with $FeBr_2$ in CH_3CN under inert atmosphere to afford $[Fe^{II}$(biot-et-dpa)$(OH_2)_2]Br_2$. Synthesis of the Fe^{III} complex was accomplished by allowing biot-et-dpa to react with $FeCl_3{\cdot}6H_2O$ in EtOH to yield $[Fe^{III}$(biot-et-dpa)$(OH_2)_3]Cl_3$. The ArMs containing the Fe^{II} complex, $[Fe^{II}$(biot-et-dpa$(OH_2)_2(\kappa^1$-$O_{E112})\subset$2xm-S_{112}E-Sav] (**1**, eq 1), and the corresponding Fe^{III}

$$\left[Fe^{II}(\text{biot-et-dpa})(OH_2)_2\right]Br_2 \xrightarrow[\substack{\text{phosphate buffer}\\ N_2,\ rt}]{\text{2xm-S}_{112}\text{E-Sav}} \underset{(1)}{\left[Fe^{II}(\text{biot-et-dpa})(OH_2)_2\left(K^1\text{-}O_{E_{112}}\right) \subset \text{2xm-S}_{112}\text{E-Sav}\right]} \quad (1)$$

complex, $[Fe^{III}$(biot-et-dpa$(X)_2(\kappa^1$-$O_{E112})\subset$2xm-S_{112}E-Sav] (**2**, eq 2), were prepared by incubating a water solution of the complexes with 2xm-S_{112}E-Sav at pH 8 in phosphate buffer (50 mM) or at pH 6 in acetate buffer (100 mM). The 2xm-S_{112}E-Sav variant is a homotetramer and to ensure complete binding of the Fe complexes a 2-(4'-hydroxyazo-benzene)benzoic acid (HABA) assay was performed on each ArM.[45] These studies indicated 4:1 ratio of biotinylated Fe complex to protein host for each ArM that confirmed complete occupancy within the Sav homotetramer (Figure S1).

$$\left[Fe^{III}(\text{biot-et-dpa})(OH_2)_3\right]Cl_3 \xrightarrow[\substack{\text{acetate buffer}\\ \text{rt}}]{\text{2xm-S}_{112}\text{E-Sav}} \underset{\substack{(2)\\ X=OH_2,\ OAc^-}}{\left[Fe^{III}(\text{biot-et-dpa})(X)_2\left(k^1\text{-}O_{E112}\right) \subset \text{2xm-S}_{112}\text{E-Sav}\right]} \quad (2)$$

Electronic absorbance and EPR spectroscopies were used to characterize 1 and 2 in solution. For **1**, one feature at λ_{max} (ε_M, $M^{-1}cm^{-1}$) = 375 (700) nm was observed with the band arising from a pyridine-to-FeII charge transfer transition (Figure S2A). For **2**, three absorbance bands were found at λ_{max} (ε_M, $M^{-1}cm^{22121}$) = 350 (2500), 485 (220), and 650 (50) nm (Figure S2B). The parallel-mode, X-band EPR spectrum for **1** displayed a broad signal with a g-value at 8.8 that is consistent with a high spin Fe^{II} species with an S = 2 spin ground state (Figure S3A). The perpendicular-mode, X-band EPR spectrum of **2** revealed weak features with g-values at 9.1 and 4.3 which are consistent with the presence of high-spin Fe^{III} species in a rhombic coordination geometry (Figure S3B). Further details on the magnetic properties of these proteins will be described in a subsequent report.

Structural Characterization of 1.

A significant advantage of utilizing biotin-Sav technology in the design of ArMs is the strong tendency of Sav to form crystals, which gives us the ability to obtain molecular structures using X-ray diffraction (XRD) methods. In general, the high affinity of biotin for Sav allows for *in crystallo* preparation of Fe ArMs by incubation of apo-Sav crystals with a solution of biotinlyated Fe complexes. For biotinylated complexes, this soaking method should generate single crystals of Sav that contain one complex per subunit. An added benefit of this approach is that we can explore chemistry performed within a single crystal that can be compared to similar processes in solution.

Single crystals of **1** were prepared by soaking crystals of apo-2xm-S_{112}E-Sav with $[Fe^{II}(\text{biot-et-dpa})(OH_2)_2]Br_2$. Its structure was solved to a resolution of 1.47 Å to reveal a mononuclear Fe complex immobilized within each subunit in which the Fe center is coordinated by O-atoms from the carboxylate group of S_{112}E bound in a κ^1 fashion and two aqua ligands (Figure 3, Tables 1 & 2, Tables S1 & S2). Nitrogen donors N1 and N2 from dpa also bind to the Fe center with Fe–N1 and Fe–N2 bond lengths of 1.94 Å and 2.32 Å. Our structure showed two conformations of the pyridine ring containing N3 (Figure 3A). The major complex (**1a**) was modelled to 70% occupancy and it was found that this pyridine ring is not coordinated (unbound state); instead N3 is H-bonded to the aqua ligand of O3. The resultant complex is 5-coordinate with a square pyramidal geometry and a τ-value of 0.05 (Figure 3B). The minor complex (**1b**) that was modelled to 30% occupancy is 6-coordinate in which N3 is bound to the Fe center (bound state) with an Fe–N3 bond length of 2.21 Å and N2–Fe–N3 and N3–Fe–O3 bond angles of 107° and 79° (Figure 3C). The carboxylate group at S_{112}E also has two conformations. In this case, the major confirmation placed O1 in a position to coordinate to the Fe center and was modelled to 80% occupancy (Figure S4A). The minor species has the carboxylate not coordinated to the Fe center and has a 20% occupancy (Figure S4A).

The molecular structure of **1a** revealed an Fe site with a facial arrangement of two N-atom donors from dpa and the O-atom from the residue of $S_{112}E$ that is similar to the 2-His-1-carboxylate facial triad observed in all non-heme monooxygenases. In addition, the κ^1-coordination of the glutamate residue in 1a and 1b leaves O4 positioned to H-bond with the aqua ligand of O2 as gauged by the O4…O2 distance of 2.71 Å. This type of monodentate carboxylate coordination to Fe with an additional intramolecular H-bond is seen in several native non-heme enzymes, such as deacetoxy-cephalosporin C synthase (Figure 1A),[12] phenylalanine hydroxylase binary enzyme (PDB: 1J8U),[46] and soybean lipoxygenase (PDB: 1JNQ).[14] These enzymes have O…O distances that range between 2.5 and 3.6 Å. The structures of the Fe^{II} complex in **1** and Fe^{II} sites in natural enzymes also share the coordination of multiple coordinated water molecules to their Fe^{II} centers.

The 2xm-S_{112}E-Sav host in **1** also promotes other non-covalent interactions with the artificial Fe cofactor. For instance, the aqua ligand with O2 has an additional H-bond that involves a structural water molecule (Wat22) that is also H-bonded to the residue of N_{49} and the backbone carbonyl of A_{86}. This aqua ligand thus participates in two H-bonds which could account for the slightly longer Fe–O3 bond length of 2.22 Å when compared to that found for the Fe–O2 bond (2.17 Å). These water molecules are also part of a larger H-bonding network that extends from N3 to the glutamate 112 side-chain and help in stabilizing its coordination to the Fe center (Figures 3B, C). Furthermore, the non-coordinating pyridine ring participates in an additional **π**-stacking interaction with the residue of W_{120} from the adjacent subunit with a $centroid_{py}$– $centroid_{trp}$ distance of 4.86 Å that likely contributes to the stabilization of this conformation (Figure 3D).

In synthetic complexes, dpa binds solely as a tridenate ligand to $Fe^{II/III}$ centers. In fact, analysis of all the structures in the Cambridge Structural Database[47] for complexes containing Fe(dpa) fragments (over 300 entries) found that both pyridine N-atoms are bound to the Fe center in the crystalline phase. Confinement of $[Fe^{II}$(biot-et-dpa)$(OH_2)_2]Br_2$ within 2xm-S_{112}E-Sav appears to promote the unusual bidentate coordination of dpa. The trapping of this Fe^{II} species with a non-coordinating pyridine ligand highlights the importance of the local environment around a metal center and how it can influence the structure of the embedded metal complex.

Structural Characterization of biot-et-dpa ⊂ 2xm-S_{112}E-Sav.

The unusual molecular structure of the Fe complexes in **1** prompted us to examine the structure of 2xm-S_{112}E-Sav containing just biot-et-dpa. We were interested in determining how the dpa ligand was positioned within the protein host in the absence of the Fe center and to examine if any structural differences occurred upon coordination to Fe. The structure of biot-et-dpa ⊂ 2xm-S_{112}E-Sav was solved to a resolution of 1.35 Å and both the dpa ligand and carboxylate group at position 112 were modelled with single conformations at 100% occupancy (Figure 4A, Tables S1 & S2). Both N1 and N2 are centered near the carboxylate group at position 112 and the pyridine ring containing N3 adopts a nearly identical confirmation to what is found in **1a**, including the same **π**-stacking interaction with W120 (Figure 4C). Additional non-covalent interactions are present in the form of an extended H-bonding network that includes N1 and N3, a series of water molecules, and the

side chains of N_{49} and $S_{112}E$ (Figure 4A). Atom N3 thus forms a H-bond as in **1a** but with a structural water molecule rather than an aqua ligand. Notice that the H-bonding network also links N3 to the carboxylate group at $S_{112}E$ which influences its orientation.

The structure found of biot-et-dpa ⊂ 2xm-S_{112}E-Sav provide insights on how the protein host influences both the primary and secondary coordination spheres in **1** (Figures 4A, B). The glutamate and pyridine with N3 have two different conformations in the structure of **1** (Figure S4A). For the glutamate, the minor state in **1** has the carboxylate occupying the same position as that observed in biot-et-dpa ⊂ 2xm-S_{112}E-Sav that places O-atoms greater than 3.0 Å from the Fe center. In its bound state, the carboxylate group rotates toward the dpa ligand enabling O1 to coordinate to the Fe center. Moreover, the placement of unbound pyridine in **1a** is only displaced by 0.6 Å from the position occupied by the same ring in biot-et-dpa ⊂ 2xm-S_{112}E-Sav. This change appears to be enough to promote intramolecular H-bonding with the aqua ligand of O3 but not enough to coordinate to the Fe center (Figure 4C). For the bound state in **1b**, there is a significant change in the position of the pyridylmethyl arm that results in N3 moving over 2.0 Å in order to coordinate to the Fe_{II} center. There is also an extended H-bonding network like the one found in **1** that includes N3, several water molecules, and the S112E sidechain (Figure 4C).

Structural Characterization of 2.

To evaluate the effects of Fe oxidation on the molecular structure of the active site, we prepared single crystals of **2** by soaking crystals of apo 2xm-S_{112}E-Sav with $[Fe^{III}$(biot-et-dpa)$(OH_2)_3]Cl_3$. Analysis of crystals that diffracted to a 1.40 Å resolution again revealed the formation of a six-coordinate mononuclear Fe complex within each subunit of Sav (Figure 5, Tables 1 & 2, Tables S3 & S4). The primary coordination sphere is composed of an N_3O_3 donor set with an O-atom donor from the residue of $S_{112}E$ that is bound in a similar κ^1 manner as observed in **1**. The other O-atom donors are from acetate ions (from the crystallization condition) that also bind as monodentate ligands and occupy the same coordination sites as the aqua ligands in **1**. The dpa ligand binds facially to the Fe^{III} center and all three N-donors are coordinated. Notice that the structural water molecule (Wat22) that was found in **1** is not present in **2** which allows O6 of the acetato ligand to H-bond with the amide residue of N_{49}, with a N_{49}…O6 distance of 2.97 Å.

To evaluate if photoreduction was occurring on the crystals of **2** and the extent of change that would cause on the resultant structure, XRD data was also collected using an X-ray free electron laser (XFEL). This technique utilizes femtosecond X-ray pulses to collect XRD data in a serial fashion with each diffraction image obtained from a new crystal.[48–51] Detection occurs before the diffusion of radicals or solvated electrons that often causes X-ray-induced changes in protein structures. Therefore, this method has provided structural data for metal centers in a non-damaged (that is, not photoreduced) state for several metalloproteins.[48–51] We were able to obtain a molecular structure of **2** that was resolved to 1.50 Å (Tables S3 & S4). The structures of **2** obtained from frozen crystals by XRD and room temperature crystals with the XFEL produced the molecular structures that were identical (Figure S4D) with an average difference in the Fe– N/O bond lengths of 0.03 Å. Notice that there is a slight difference in the orientations of the ligands in the two structures

(Figure 5B) which could be caused by the different temperatures that were used for data collection. Nevertheless, these results suggest that the structure of **2** obtained using synchrotron radiation at cryogenic temperatures had only limited radiation damage.

X-ray Absorption Spectroscopy.

The properties of the Fe center in **1** were further probed using X-ray absorption spectroscopy (XAS) to gain a better understanding of the structure of protein-embedded complex in solution (see SI, Figures S5–S7). X-ray absorption near edge structure (XANES) analysis provided an energy edge for **1** at 7122.4 eV (Figure S7), which is consistent with an Fe^{II} center.[52–54] Extended X-ray absorption fine structure (EXAFS) analysis revealed that for **1** there are five O/N scatterers at a distance of 2.15 Å (Table 3, Tables S5-S6). Two additional shells from the Fe center were fit to four carbon scatterers at 3.01 Å and one at 2.63 Å. The longer distance carbon scatterers could include the carbonyl C-atom of $S_{112}E$ side-chain which is found at Fe…C distance of 3.12 Å by XRD. The shorter distance Fe…C distance of 2.60 Å matched that found by XRD for the Fe center to the methylene carbon of the unbound pyridylmethyl group. Taken together, these data suggest that the predominate species in solution for **1** is also the unbound state in which one pyridine ring of dpa is not coordinated (Figure 3B).

Azide Binding to 2.

We chose to examine the binding of azide ions to **2** in order to investigate how exogenous ligands bind to the Fe center. In solution studies, **2** was treated with a 100-fold excess of NaN_3 in acetate buffer pH 6 to afford a new spectrum with a band at a λ_{max} (ε_M, $M^{-1}cm^{-1}$) = 405 (3000) nm that is assigned to an azido-to-Fe^{III} charge transfer transition (Figure 6A, S8).[55] Parallel *in crystallo* studies were performed that involved soaking crystals of **2** in a 100 mM solution of NaN3 to afford **2**–N_3, whose structure was obtained to a resolution of a 1.85 Å (Figure 6B,C). Analysis of the molecular structure of **2**–N_3 revealed a monomeric Fe complex where the dpa ligand, the carboxylate side chain of $S_{112}E$, and one acetato ligand containing O3 are coordinated in the same positions as found in **2** (Figures 6B, C). However, the second acetato ligand is absent. In its place is electron density that we have modelled as a terminal azido ligand with an Fe–N4 bond length of 2.15 Å. The azido ligand has an Fe–N4–N5 bond angle of 120.1° that is comparable to bond angles found in previously reported Fe^{III}–N_3 complexes.[56] The presence of the azido ligand in **2**–N3 causes an 0.29 Å elongation of Fe–N2 bond distance compared to what is observed in **2**, which is consistent with an azido ligand having a stronger trans-influence than an acetate ion. The structural water molecule Wat1is modelled at 100% occupancy and is part of an H-bonding network that includes the azido ligand. The H-bonding network extends from the proximal N4 of the azido ligand and includes Wat1, and the amide residue of N_{49} with N4·Wat1 and Wat1·N_{49} distances of 2.88 and 3.17 Å, respectively (Figure 6B).

Summary and Conclusions

The results from these studies on our new Fe proteins further illustrates the versatility of using biotin-Sav technology to engineer ArMs. Our approach leverages the proper placement of synthetic complexes proximal to endogenous functional groups to produce new

biomimetic constructs. We utilized knowledge gained from our previous work on Cu proteins, which revealed that an ethylene linker between a metal complex and the biotin positioned the Cu center near the side-chain at position 112. Following this design concept, the Sav protein was re-engineered to produce the host 2xm-S_{112}E-Sav which included a glutamate at position 112. When matched with the biotinylated complexes, [Fe^{II}(biot-et-dpa)$(OH_2)_2$]Br_2 and [Fe^{III}(biot-et-dpa)$(OH_2)_3$]Cl_3, ArMs were produced with properties that resemble those found in mononuclear non-heme iron enzymes. The positioning of the artificial cofactors within 2xm-S_{112}E-Sav allow for monodentate coordination of the carboxylate side-chain in an identical manner as found in the active sites of Fe monooxygenases. Moreover, the unusual structural finding in **1a**, in which one pyridine group of the dpa ligand is not coordinated, produced an Fe binding that is similar to the 2-His-1-carboxylate facial triad found in the natural metalloproteins. The observation that only one pyridine group is coordinated to the Fe center in **1a** is unusual and has not been structurally observed in other Fe complexes with dpa. We attribute this difference to the confinement of the complex within a protein host that help regulate the secondary coordination sphere around the Fe complexes. In fact, there are several non-covalent interactions to the complexes that include those with a pyridine ring of the dpa ligand that stabilizes the unbound state found in **1a**. An additional H-bond was found between an aqua ligand and the noncoordinating O-atom of a glutamate side-chain, an interaction that is found in many non-heme Fe enzymes.

The structure of **2** also revealed a κ^1–coordination to the FeIII center of the carboxylate at position 112. In **2**, the Fe complex is 6-coordinate and the aqua ligands have been replaced with acetato ligands to produce a primary coordination sphere that contains three monodentate carboxylate ligands. Again, H-bonds involving the carboxylate ligands appear to help stabilize this unusual coordination environment. Substitution of the one of the acetato ligands was achieved by treating **2** with excess azide ion to produce **2**–N_3. The structure of **2**–N_3, along with those of **1** and **2**, also illustrate the importance of the amide side-chain of N49 in maintaining H-bonding networks around the complexes. Taken together, our findings highlight how the synergistic design of Sav and an artificial metallocofactor allow for the control of both the primary and secondary coordination spheres of a confined metal complex within a protein host.

Experimental

General Methods.

All commercially available reagents were obtained of the highest purity and used as received. Acetonitrile (CH3CN), Ethanol (CH_3CH_2OH) and diethylether were degassed with argon and dried by vacuum filtration through activated alumina according to the procedure by Grubbs.[57] Triethylamine was distilled from KOH. Thin-layer chromatography (TLC) was performed on Merck 60 F254 aluminum-backed silica plates or Merck 60 F254 glass-backed basic aluminum oxide plates. Eluted plates were visualized using UV light. Silica or basic alumina gel chromatography was performed with the indicated solvent system using Fisher reagent silica gel 60 (230–400 mesh) or Sigma reagent Brockmann 1 basic aluminum oxide

58 (150 mesh). Biotin pentafluorophenol ester (biot-PFP)[58] and di-(2-picolyl)amine[59] were prepared according to literature procedures.

2-(2-(bis(pyridin-2-ylmethyl)amino)ethyl)isoindoline-1,3-dione (1).[42]

Dpa (2.03 g, 10.0 mmol), bromoethylphthalimide (2.93 g, 11.0 mmol), KI (0.339 g, 0.002 mol) and K_2CO_3 (5.6 g, 41 mmol) were dissolved in 60 mL acetonitrile and refluxed for 24 hours. The solution was cooled to room temperature, filtered, and reduced to dryness. The maroon-brown residue was dissolved in 30 mL dichloromethane and washed with 3 × 30 mL aqueous $NaHCO_3$ (with a small addition of brine) and 2 × 30 mL water. The maroon-brown organic layer was acidified with 20 mL 12 mM HCl dissolved in 10 mL water and washed with 5 × 30 mL dichloromethane. The aqueous layer was carefully neutralized with solid $NaHCO_3$ and extracted with 4 × 30 mL dichloromethane. The solution was dried with $MgSO_4$, filtered and reduced to dryness to yield a red-brown oil. The crude product was purified via column chromatography with silica gel and methanol:dichloromethane:Et_3N (9:90:1) or with basic alumina and methanol:dichloromethane (10:90) as the eluent to yield pure **1** as a yellow oil (1.68 g, 44%–50%). ^1H (500 mHz, $CDCl_3$) δ 8.44 (d, 2H), 7.82 (dd, 2H), 7.74 (dd, 2H) 7.42 (t, 2H), 7.34 (d, 2H), 7.06 (t, 2H), 3.85 (m, 6H), 2.86 (t, 2H). MS (ESI, MeOH) *m/z* calcd $C_{22}H_{20}N_4O_2$ [M + (Na^+)] 395.15, found 395.09.

N,N-bis(pyridin-2-ylmethyl)ethane-1,2-diamine (2).[42]

Hydrazine monohydrate (1.10 mL, 0.020 mol) and **1** (1.7 g, 5.0 mmol) were dissolved in 60 mL ethanol and refluxed under N_2 for 3 hours. The phthalhydrazide byproduct precipitated as a white solid after 15 minutes of reflux. The solution was filtered to remove the phthalhydrazide and washed with 3 × 5 mL chloroform. The solution was reduced to dryness and the yellow oily residue was dissolved in 40 mL chloroform and 40 mL of 1 M NaOH. The aqueous layer was extracted with 3 × 40 mL chloroform, dried over $MgSO_4$, filtered, and reduced to dryness. The product **2** was recovered as a yellow oil (0.80 g, 77%). ^1H (500 mHz, $CDCl_3$) δ 8.53 (d, 2H), 7.66 (t, 2H), 7.50 (d, 2H) 7.15 (t, 2H), 3.85 (s, 4H), 2.80 (t, 2H), 2.66 (t, 2H). MS (ESI, MeOH) *m/z* calcd $C_{14}H_{18}N_4$ [M + (H^+)] 243.16, found 243.11.

Biot-ethyl-dpa (3).[42]

A solution of biot-PFP (1.30 g, 3.01 mmol), **2** (0.85 g, 3.0 mmol), and triethylamine (0.39 g, 3.0 mmol) in 20 mL DMF was allowed to stir overnight. The DMF was removed under vacuum to yield a sticky tan residue. The residue was triterated with diethylether until a free-flowing solid formed (3–7 days). The light tan solid was filtered, washed with diethylether, and dried under vacuum (1.49 g, 91%). The solid **3** was stored under an inert atmosphere. ^1H (500 mHz, DMSO) δ 8.44 (d, 2H), 7.75 (br, 1H), 7.71 (t, 2H) 7.50 (d, 2H), 7.21 (t, 2H), 6.40 (s, 1H), 6.33 (s, 1H), 4.27 (t, 1H), 4.07 (t, 1H), 3.72 (s, 4H), 3.16 (q, 2H), 3.04 (q, 1 H), 2.78 (dd, 1 H), 2.55 (s, 1H), 2.46 (t, 2H), 2.02 (t, 2H), 1.45 (m, 6H). MS (ESI, MeOH) *m/z* calcd $C_{24}H_{32}N_6O_2S$ [M + (Na^+)] 491.22, found 491.17.

Preparation of Metal Complexes

$[Fe^{II}$(biot-ethyl-dpa)$(OH_2)_2]Br_2$.[60]: $[Fe^{II}$(Biot-ethyl-DPA)$(OH_2)_2]Br_2$ was prepared by addition of **3** (53 mg, 0.24 mmol) in 10 mL acetonitrile to $FeBr_2$. A pale yellow solid

immediately precipitated from the solution. The suspension was allowed to stir under N_2 for 30 mins, after which the pale-yellow solid was collected via filtration, washed with CH_3CN:diethyl ether (1:1), and dried under vacuum (0.125 g, 75%). The solid was stored under an inert atmosphere. HR-MS (ESI, 1% DMF:MeCN) m/z calcd for $C_{24}H_{32}FeN_6O_2SBr$ [M – (Br–)] 603.08, found 603.08. Elem. Anal. Calcd for ($C_{24}H_{36}N_6SO_4FeBr_2$): C, 40.02; H, 5.04; N, 11.67. Found: C, 39.67; H, 4.52; N, 11.38.

[Fe^{III}(biot-ethyl-dpa)(OH_2)$_3$]Cl_3.[61]: [Fe^{III}(Biot-ethyl-DPA)(OH_2)$_3$]Cl_3 was prepared by addition of **3** (0.09 g, 0.2 mmol) in 3 mL ethanol to $FeCl_3 \cdot 6H_2O$ (0.10 g, 0.38 mmol) in 3 mL ethanol. A yellow solid immediately precipitated from the solution. The suspension was allowed to stir under N_2 for 15 minutes, after which the yellow solid was isolated via filtration. The solid was washed with 10 mL chilled ethanol:ether (4:1) and dried under vacuum (0.10 g, 86%). The solid was stored under an inert atmosphere. HR-MS (ESI, MeOH) *m/z* calcd for $C_{24}H_{32}Cl_2FeN_6O_2S$ [M – (Cl–)] 594.10, found 594.08. Elem. Anal. Calcd for ($C_{24}H_{38}N_6SO_5FeCl_3$): C, 42.09; H, 5.59; N, 12.27. Found: C, 42.28; H, 5.12; N, 12.23.

Analytical and Spectroscopic Methods.

HABA Titrations.—To 2.4 mL of 8 μM Sav in 200 mM sodium phosphate buffer at pH 7 was added 300 μL of a 10 mM 2-(4′-hydroxyazobenzene)benzoic acid (HABA) in 200 mM phosphate buffer pH 7. After 5 min equilibration, the absorbance at 506 nm was recorded. A solution of 1 mM Fe complex in nanopure water was added in 4–20 μL portions until approximately 4 equivalents had been added. The absorbance at 506 nm was recorded until no further changes in intensity were observed.

Electronic Absorption Studies.—A solution of lyophilized protein (50–250 μM) was prepared in nanopure water. Four equivalents of Fe complex (0.2–1 mM) in nanopure water were added to the protein solution. Samples were diluted to their final concentrations in a final volume of 500 uL containing 50 mM potassium phosphate or 100 mM sodium acetate buffer at the indicated pH.

EPR Studies.—A solution of protein (500 μM) was prepared in nanopure water. Four equivalents of Fe complex (2 mM) in nanopure water were added to the protein solution. Samples were diluted to their final concentrations in a final volume of 300 uL containing 50 mM potassium phosphate or 100 mM sodium acetate buffer at the indicated pH. The sample was transferred to an EPR tube, frozen at 77 K in liquid nitrogen and run at 10 K.

XAS Studies.—A solution of protein (750 μM) was prepared in nanopure water. Four equivalents of Fe complex (3 mM) in nanopure water were added to the protein solution. Samples were diluted to their final concentrations in a final volume of 250 uL with nanopure water. The sample was then poured in liquid ethane to freeze and packed as a solid into a pre-cooled XAS sample holder.

Protein Crystallization

Crystallization of [Fe^{II}(biot-et-dpa(OH_2)$_2$(κ^1-O_{E112})⊂2xm-S_{112}E-Sav].: Apo-Sav protein was crystallized by sitting drop vapor diffusion method under an inert atmosphere. Diffraction quality crystals were grown at room temperature by mixing 3.5 μL of protein solution (26 mg/mL lyophilized protein in water) and 1.5 μL of crystallization buffer (2.0 ammonium sulfate, 0.1 M sodium acetate, pH 4). The droplet was equilibrated against a reservoir solution of 100 uL crystallization buffer. Single crystals of Sav were prepared by soaking apo-crystals in a soaking buffer (2.6 ammonium sulfate, 0.1 M sodium acetate, pH 8) with a 10 mM stock solution of [Fe^{II}(Biot-et-DPA)(OH_2)$_2$]Br_2 in nanopure water (9 μL crystallization buffer, 1 μL [Fe^{II}(biot-et-dpa)(OH_2)$_2$]Br_2) overnight. After the soaking, crystals were transferred to cryo-protectant for 1 min (30% glycerol in crystallization buffer) and shock-frozen in liquid nitrogen.

Crystallization of [Fe^{III}(biot-et-dpa(OAc)$_2$(κ^1-O_{E112})⊂2xm-S_{112}E-Sav].: Apo-Sav protein was crystallized by sitting drop vapor diffusion method. Diffraction quality crystals were grown at room temperature by mixing 3.5 μL of protein solution (26 mg/mL lyophilized protein in water) and 1.5 μL of crystallization buffer (2.0 ammonium sulfate, 0.1 M sodium acetate, pH 4). The droplet was equilibrated against a reservoir solution of 100 uL crystallization buffer. Single crystals of Sav were prepared by soaking apo-crystals in a soaking buffer (2.6 ammonium sulfate, 0.1 M sodium acetate, pH 6) with a 10 mM stock solution of [Fe^{III}(biot-ethyl-dpa)(OH_2)$_3$]Cl_3 in nanopure water (9 μL crystallization buffer, 1 μL [Fe^{III}(biot-ethyl-dpa)(OH_2)$_3$]Cl_3) overnight. After the soaking, crystals were transferred to cryo-protectant for 1 min (30% glycerol in crystallization buffer) and shock-frozen in liquid nitrogen. Crystals were prepared in the same manner for data collected using XFEL.

Crystallization of biot-et-dpa⊂ 2xm-S112E-Sav.: Apo-Sav protein was crystallized by sitting drop vapor diffusion method. Diffraction quality crystals were grown at room temperature by mixing 3.5 μL of protein solution (26 mg/mL lyophilized protein in water) and 1.5 μL of crystallization buffer (2.0 ammonium sulfate, 0.1 M sodium acetate, pH 4). The droplet was equilibrated against a reservoir solution of 100 uL crystallization buffer. Single crystals of Sav were prepared by soaking apo-crystals in a soaking buffer (2.6 ammonium sulfate, 0.1 M sodium acetate, pH 6) with a 10 mM stock solution of biot-et-dpa in nanopure water (9 μL crystallization buffer, 1 μL biot-et-dpa) overnight. After the soaking, crystals were transferred to cryo-protectant for 1 min (30% glycerol in crystallization buffer) and shock-frozen in liquid nitrogen.

Crystallization of [Fe^{III}(biot-ethyl-dpa)(OAc)(N_3)(κ^1-O_E)⊂ 2xm-S_{112}E-Sav].: Apo-Sav protein was crystallized by sitting drop vapor diffusion method. Diffraction quality crystals were grown at room temperature by mixing 3.5 μL of protein solution (26 mg/mL lyophilized protein in water) and 1.5 μL of crystallization buffer (2.0 ammonium sulfate, 0.1 M sodium acetate, pH 4). The droplet was equilibrated against a reservoir solution of 100 uL crystallization buffer. Single crystals of Sav were prepared by soaking apo-crystals in a soaking buffer (2.6 ammonium sulfate, 0.1 M sodium acetate, pH 6) with a 10 mM stock solution of [Fe^{III}(biot-ethyl-dpa)(OH_2)$_3$]Cl_3 in nanopure water (9 μL crystallization buffer, 1 μL [Fe^{III}(biot-ethyl-dpa)(OH_2)$_3$]Cl_3) overnight. After this initial soaking, crystals were

again soaked in a soaking buffer (2.6 ammonium sulfate, 0.1 M sodium acetate, pH 6) with a 1 M stock solution of NaN_3 in nanopure water for 5–10 mins (9 μL crystallization buffer, 1 μL NaN_3). After the second soaking, the crystals were transferred to cryo-protectant for 1 minute (30% glycerol in crystallization buffer) and shock-frozen in liquid nitrogen.

Physical Methods

Instrumentation.—^{1}H, ^{13}C, and ^{19}F NMR spectra were recorded at 500/600, 125, and 400 MHz, respectively. ^{1}H NMR spectra were reported in ppm on the δ scale and referenced to tetramethylsilane or solvent residual. The data are presented as follows: chemical shift, multiplicity (s = singlet, d = doublet, t = triplet, q = quartet, quin = quintet, m = multiplet, br = broad), and integration. Mass spectra were measured on a MicroMass AutoSpec E, a MicroMass Analytical 7070E, or a MicroMass LCT Electrospray instrument. Electronic absorbance spectra were recorded with a Cary 50 or 8453 Agilent UV-vis spectrophotometer. X-band (9.64 GHz) EPR spectra were recorded on a Bruker spectrometer equipped with Oxford liquid helium cryostats. The quantification of all signals is relative to a CuEDTA spin standard. The concentration of the standard was derived from an atomic absorption standard (Aldrich). For all instruments, the microwave frequency was calibrated with a frequency counter and the magnetic field with an NMR gaussmeter. A modulation frequency of 100 kHz was used for all EPR spectra. The EPR simulation software (SpinCount) was written by our collaborating author Michael P. Hendrich.[62]

Supplementary Material

Refer to Web version on PubMed Central for supplementary material.

ACKNOWLEDGMENT

We thank the National Institutes of Health USA (GM120349 to A.S.B., GM101390 to M.T.G., GM110501 to J.Y., GM126289 to J.K. and GM117126 to N.K.S.)) for financial support. K.R.M. acknowledges the National Science Foundation Graduate Research Fellowship (NSF-GRFP I.D. 2015203061) for financial support. Use of the Linac Coherent Light Source (LCLS) at the SLAC National Accelerator Laboratory were supported by the U.S. Department of Energy (DOE), Office of Science, Office of Basic Energy Sciences under Contract No. DE-AC02–76SF00515, and the Advanced Light Source at Lawrence Berkeley National Laboratory (ALS-09183, ASB) for support of this work. Data processing for the XFEL study was performed in part at the National Energy Research Scientific Computing Center, supported by the DOE Office of Science, Contract No. DEAC02–05CH11231.

References

(1). Solomon EI; Brunold TC; Davis MI; Kemsley JN; Lee S-K; Lehnert N; Neese F; Skulan AJ; Yang Y-S; Zhou J. Geometric and Electronic Structure/Function Correlations in Non-Heme Iron Enzymes. Chem. Rev 2000, 100, 235–350. [PubMed: 11749238]

(2). Kal S; Que L. Dioxygen Activation by Nonheme Iron Enzymes with the 2-His-1-Carboxylate Facial Triad That Generate High-Valent Oxoiron Oxidants. J. Biol. Inorg. Chem 2017, 22, 339–365. [PubMed: 28074299]

(3). Bruijnincx PCA; van Koten G; Gebbink RJMK Mononuclear Non-Heme Iron Enzymes with the 2-His-1-Carboxylate Facial Triad: Recent Developments in Enzymology and Modeling Studies. Chem. Soc. Rev 2008, 37, 2716–2730. [PubMed: 19020684]

(4). Kovaleva EG; Lipscomb JD. Versatility of Biological Non-Heme Fe(II) Centers in Oxygen Activation Reactions. Nat. Chem. Biol 2008, 4, 186–193. [PubMed: 18277980]

(5). Bugg TD; Ramaswamy S. Non-Heme Iron-Dependent Dioxygenases: Unravelling Catalytic Mechanisms for Complex Enzymatic Oxidations. Curr. Opin. Chem. Biol 2008, 12, 134–140. [PubMed: 18249197]

(6). Davis KM; Altmyer M; Martinie RJ; Schaperdoth I; Krebs C; Bollinger JM; Boal AK. Structure of a Ferryl Mimic in the Archetypal Iron(II)- and 2-(Oxo)-Glutarate-Dependent Dioxygenase, TauD. Biochemistry 2019, 58, 4218–4223. [PubMed: 31503454]

(7). Bollinger JM; Price JC; Hoffart LM; Barr EW; Krebs C. Mechanism of Taurine: α-Ketoglutarate Dioxygenase (TauD) from Escherichia Coli. European Journal of Inorganic Chemistry. 11 4, 2005, pp 4245–4254.

(8). Hausinger RP. Fe(II)/α-Ketoglutarate-Dependent Hydroxylases and Related Enzymes. Crit. Rev. Biochem. Mol. Biol 2004, 39, 21–68. [PubMed: 15121720]

(9). Koehntop KD; Emerson JP; Que LJ. The 2-His-1-Carboxylate Facial Triad: A Versatile Platform for Dioxygen Activation by Mononuclear Non-Heme Iron(II) Enzymes. J. Biol. Inorg. Chem 2005, 10, 87–93. [PubMed: 15739104]

(10). Costas M; Mehn MP; Jensen MP; Que LJ. Dioxygen Activation at Mononuclear Nonheme Iron Active Sites: Enzymes, Models, and Intermediates. Chem. Rev 2004, 104, 939–986. [PubMed: 14871146]

(11). Hegg EL; Que L. The 2-His-1-Carboxylate Facial Triad - An Emerging Structural Motif in Mononuclear Non-Heme Iron(II) Enzymes. Eur. J. Biochem 1997, 250, 625–629. [PubMed: 9461283]

(12). Valegard K; Terwisscha van Scheltinga AC; Lloyd MD; Hara T; Ramaswamy S; Perrakis A; Thompson A; Lee H-J; Baldwin JE; Schofield CJ; Andersson JH; Anderrson I. Structure of a Cephalosporin Synthase. Nature 1998, 394, 805–809. [PubMed: 9723623]

(13). Elkins JM; Ryle MJ; Clifton IJ; Dunning Hotopp JC; Lloyd JS; Burzlaff NI; Baldwin JE; Hausinger RP; Roach PL. X-Ray Crystal Structure of Escherichia Coli Taurine/α-Ketoglutarate Dioxygenase Complexed to Ferrous Iron and Substrates. Biochemistry 2002, 41, 5185–5192. [PubMed: 11955067]

(14). Minor W; Steczko J; Stec B; Otwinowski Z; Bolin JT; Walter R; Axelrod B. Crystal Structure of Soybean Lipoxygenase L-1 at 1.4 Å Resolution. Biochemistry 1996, 35, 10687–10701. [PubMed: 8718858]

(15). Ha EH; Ho RYN; Krisiel JF; Valentine JS. Modeling the Reactivity of α-Ketoglutarate-Dependent Non-Heme Iron(II)-Containing Enzymes. Angew. Chem., Int. Ed 1995, 34, 2265–2266.

(16). Oldenburg PD; Ke CY; Tipton AA; Shteinman AA; Que L. A Structural and Functional Model for Dioxygenases with a 2-His-1-Carboxylate Triad. Angew. Chem., Int. Ed 2006, 45, 7975–7978.

(17). Chiou Y-M; Que L. Models for α-Keto Acid-Dependent Non-Heme Iron Enzymes: Structures and Reactivity of [FeII(L)(O2CCOPh)](ClO4) Complexes. J. Am. Chem. Soc 1995, 117, 3999–4013.

(18). Chiou YM; Que L. Model Complexes for α-Keto Acid-Dependent Enzymes. Structure and Reactivity of {FeII[Tris[(6-Methyl-2-Pyridyl)Methyl]Amine](Benzoylformate)}(ClO4). J. Am. Chem. Soc 1992, 114, 7567–7568.

(19). Chiou Y. -M; Que, L. A Model for α-Keto Acid Dependent Nonheme Iron Enzymes: Structure and Reactivity of [Fe2II(Me2Hdp)2(Bf)](ClO4). Angew. Chem., Int. Ed 1994, 33, 1886–1888.

(20). Hagadorn JR; Que J; Tolman WB. N-Donor Effects on Carboxylate Binding in Mononuclear Iron(II) Complexes of a Sterically Hindered Benzoate Ligand. Inorg. Chem 2000, 39, 6086–6090. [PubMed: 11188526]

(21). Kitajima N; Moro-oka Y; Tamura N; Amagai H; Fukui H; Mizutani Y; Mathur R; Heerwegh K; Reed CA; Randall CR; Tatsumi K. Monomelic Carboxylate Ferrous Complexes as Models for the Dioxygen Binding Sites in Non-Heme Iron Proteins. The Reversible Formation and Characterization of μ-Peroxo Diferric Complexes. J. Am. Chem. Soc 1994, 116, 9071–9085.

(22). Bruijnincx PCA; Lutz M; Spek AL; Hagen WR; Weckhuysen BM; Van Koten G; Gebbink RJMK Modeling the 2-His-1-Carboxylate Facial Triad: Iron-Catecholato Complexes as Structural and

Functional Models of the Extradiol Cleaving Dioxygenases. J. Am. Chem. Soc 2007, 129, 2275–2286. [PubMed: 17266307]

(23). Moelands MAH; Nijsse S; Folkertsma E; De Bruin B; Lutz M; Spek AL; Gebbink RJMK Bioinspired Nonheme Iron Complexes Derived from an Extended Series of N,N,O-Ligated BAIP Ligands. Inorg. Chem 2013, 52, 7394–7410. [PubMed: 23750826]

(24). Folkertsma E; De Waard EF; Korpershoek G; Van Schaik AJ; Solozabal Mirón N; Borrmann M; Nijsse S; Moelands MAH; Lutz M; Otte M; Moret ME; Gebbink RJMK Mimicry of the 2-His-1-Carboxylate Facial Triad Using Bulky N,N,O-Ligands: Non-Heme Iron Complexes Featuring a Single Facial Ligand and Easily Exchangeable Co-Ligands. Eur. J. Inorg. Chem 2016, 1319–1332.

(25). Burzlaff N. Biomimetic Trispyrazolylborato Iron Complexes. Angew. Chem., Int. Ed 2009, 48, 5580–5582.

(26). Beck A; Weibert B; Burzlaff N. Monoanionic N,N,O-Scorpionate Ligands and Their Iron(II) and Zinc(II) Complexes: Models for Mononuclear Active Sites of Non-Heme Iron Oxidases and Zinc Enzymes. Eur. J. Inorg. Chem 2001, 521–527.

(27). Beck A; Barth A; Hubner E; Burzlaff N. Bis(Pyrazol-1-Yl)Acetates as Tripodal Heteroscorpionate Ligands in Iron Chemistry: Syntheses and Structures of Iron(II) and Iron(III) Complexes with Bpza, Bdmpza, and Bdtbpza Ligands. Inorg. Chem 2003, 42, 7182–7188. [PubMed: 14577787]

(28). Cappillino PJ; Miecznikowski JR; Tyler LA; Tarves PC; McNally JS; Lo W; Kasibhatla BST; Krzyaniak MD; McCracken J; Wang F; Armstrong WH; Caradonna JP. Studies of Iron(II) and Iron(III) Complexes with Fac-N2O, Cis-N2O2 and N2O3 Donor Ligands: Models for the 2-His 1-Carboxylate Motif of Non-Heme Iron Monooxygenases. Dalt. Trans 2012, 41, 5662–5677.

(29). Rocks SS; Brennessel WW; Machonkin TE; Holland PL. Solid-State and Proton NMR Characterization of an Iron(II) Complex of a Tridentate, Facially Coordinating N,N,O Donor Ligand. Inorganica Chim. Acta 2009, 362, 1387–1390.

(30). Dhanalakshmi T; Bhuvaneshwari M; Palaniandavar M. Iron(III) Complexes of Certain Meridionally Coordinating Tridentate Ligands as Models for Non-Heme Iron Enzymes: The Role of Carboxylate Coordination. J. Inorg. Biochem 2006, 100, 1527–1534. [PubMed: 16814389]

(31). Rittle J; Field MJ; Green MT; Tezcan FA. An Efficient, Step-Economical Strategy for the Design of Functional Metalloproteins. Nat. Chem 2019, 11, 434–441. [PubMed: 30778140]

(32). Liu J; Chakraborty S; Hosseinzadeh P; Yu Y; Tian S; Petrik I; Bhagi A; Lu Y. Metalloproteins Containing Cytochrome, Iron–Sulfur, or Copper Redox Centers. Chem. Rev 2014, 114, 4366–4469. [PubMed: 24758379]

(33). Nastri F; Chino M; Maglio O; Bhagi-Damodaran A; Lu Y; Lombardi A. Design and Engineering of Artificial Oxygen-Activating Metalloenzymes. Chem. Soc. Rev 2016, 45, 5020–5054. [PubMed: 27341693]

(34). McLaughlin MP; Retegan M; Bill E; Payne TM; Shafaat HS; Peña S; Sudhamsu J; Ensign AA; Crane BR; Neese F; Holland PL. Azurin as a Protein Scaffold for a Low-Coordinate Nonheme Iron Site with a Small-Molecule Binding Pocket. J. Am. Chem. Soc 2012, 134, 19746–19757. [PubMed: 23167247]

(35). Cavazza C; Bochot C; Rousselot-Pailley P; Carpentier P; Cherrier MV; Martin L; Marchi-Delapierre C; Fontecilla-Camps JC; Ménage S. Crystallographic Snapshots of the Reaction of Aromatic C-H with O2 Catalysed by a Protein-Bound Iron Complex. Nat. Chem 2010, 2, 1069–1076. [PubMed: 21107372]

(36). Snyder RA; Betzu J; Butch SE; Reig AJ; DeGrado WF; Solomon EI. Systematic Perturbations of Binuclear Non-Heme Iron Sites: Structure and Dioxygen Reactivity of de Novo Due Ferri Proteins. Biochemistry 2015, 54, 4637–4651. [PubMed: 26154739]

(37). Faiella M; Andreozzi C; de Rosales RTM; Pavone V; Maglio O; Nastri F; DeGrado WF; Lombardi A. An Artificial Di-Iron Oxo-Protein with Phenol Oxidase Activity. Nat. Chem. Biol 2009, 5, 882–884. [PubMed: 19915535]

(38). Wilson ME; Whitesides GM. Conversion of a Protein to a Homogeneous Asymmetric Hydrogenation Catalyst by Site-Specific Modification with a Diphosphinerhodium(I) Moiety. J. Am. Chem. Soc 1978, 100, 306–307.

(39). Ward TR. Artificial Metalloenzymes Based on the Biotin-Avidin Technology: Enantioselective Catalysis and Beyond. Acc. Chem. Res 2011, 44, 47–57. [PubMed: 20949947]

(40). Schwizer F; Okamoto Y; Heinisch T; Gu Y; Pellizzoni MM; Lebrun V; Reuter R; Köhler V; Lewis JC; Ward TR. Artificial Metalloenzymes: Reaction Scope and Optimization Strategies. Chem. Rev 2017, 118, 142–231. [PubMed: 28714313]

(41). Heinisch T; Ward TR. Artificial Metalloenzymes Based on the Biotin-Streptavidin Technology: Challenges and Opportunities. Acc. Chem. Res 2016, 49, 1711–1721. [PubMed: 27529561]

(42). Mann SI; Heinisch T; Weitz AC; Hendrich MP; Ward TR; Borovik AS. Modular Artificial Cupredoxins. J. Am. Chem. Soc 2016, 138, 9073–9076. [PubMed: 27385206]

(43). Mann SI; Heinisch T; Ward TR; Borovik AS. Peroxide Activation Regulated by Hydrogen Bonds within Artificial Cu Proteins. J. Am. Chem. Soc 2017, 139, 17289–17292. [PubMed: 29117678]

(44). Olshansky L; Huerta-Lavorie R; Nguyen AI; Vallapurackal J; Furst A; Tilley TD; Borovik AS. Artificial Metalloproteins Containing Co4O4 Cubane Active Sites. J. Am. Chem. Soc 2018, 140, 2739–2742. [PubMed: 29401385]

(45). Skander M; Humbert N; Collot J; Gradinaru J; Klein G; Loosli A; Sauser J; Zocchi A; Gilardoni F; Ward TR. Artificial Metalloenzymes: (Strept)Avidin as Host for Enantioselective Hydrogenation by Achiral Biotinylated Rhodium-Diphosphine Complexes. J. Am. Chem. Soc 2004, 126, 14411–14418. [PubMed: 15521760]

(46). Andersen OA; Flatmark T; Hough E. High Resolution Crystal Structures of the Catalytic Domain of Human Phenylalanine Hydroxylase in Its Catalytically Active Fe(II) Form and Binary Complex with Tetrahydrobiopterin. J. Mol. Biol 2001, 314, 279–291. [PubMed: 11718561]

(47). Groom CR; Bruno IJ; Lightfoot MP; Ward SC. The Cambridge Structural Database. Acta Cryst 2016, 72, 171–179.

(48). Hirata K; Shinzawa-Itoh K; Yano N; Takemura S; Kato K; Hatanaka M; Muramoto K; Kawahara T; Tsukihara T; Yamashita E; Tono K; Ueno G; Hikima T; Murakami H; Inubushi Y; Yabashi M; Ishikawa T; Yamamoto M; et al. Determination of Damage-Free Crystal Structure of an X-Ray-Sensitive Protein Using an XFEL. Nat. Methods 2014, 11, 734–736. [PubMed: 24813624]

(49). Suga M; Akita F; Hirata K; Ueno G; Murakami H; Nakajima Y; Shimizu T; Yamashita K; Yamamoto M; Ago H; Shen J-R Native Structure of Photosystem II at 1.95 Å Resolution Viewed by Femtosecond X-Ray Pulses. Nature 2014, 517, 1–17.

(50). Kern J; Yachandra VK; Yano J. Metalloprotein Structures at Ambient Conditions and in Real-Time: Biological Crystallography and Spectroscopy Using X-Ray Free Electron Lasers. Curr. Opin. Struct. Biol 2015, 34, 87–98. [PubMed: 26342144]

(51). Kern J; Tran R; Alonso-Mori R; Koroidov S; Echols N; Hattne J; Ibrahim M; Gul S; Laksmono H; Sierra RG; Gildea RJ; Han G; Hellmich J; Lassalle-Kaiser B; Chatterjee R; Brewster AS; Stan CA; Glöckner C; et al. Taking Snapshots of Photosynthetic Water Oxidation Using Femtosecond X-Ray Diffraction and Spectroscopy. Nat. Commun 2014, 5, 4371. [PubMed: 25006873]

(52). Mcdonald AR; Bukowski MR; Farquhar ER; Jackson TA; Koehntop KD; Seo MS; Hont RF. De; Stubna, A.; Halfen, J. A.; Mu, E. Sulfur versus Iron Oxidation in an Iron - Thiolate Model Complex. 2010, No. 4, 17118–17129.

(53). England J; Farquhar ER; Guo Y; Cranswick MA; Ray K; Eckard M; Que L. Characterization of a Tricationic Trigonal Bipyramidal Iron (IV) Cyanide Complex , with a Very High Reduction Potential , and Its Iron (II) and Iron (III) Congeners. 2011, No. Iv, 2885–2896.

(54). Rohde J; Shan X; Lim MH; Klinker EJ; Chen K; Nam W; Que L. Structural Insights into Nonheme Alkylperoxoiron (III) and Oxoiron (IV) Intermediates by X-Ray Absorption Spectroscopy. 2004, No. Iii, 16750–16761.

(55). Berry JF; Bill E; Bothe E; Weyhermüller T; Wieghardt K. Octahedral Non-Heme Non-Oxo Fe(IV) Species Stabilized by a Redox-Innocent N-Methylated Cyclam-Acetate Ligand. J. Am. Chem. Soc 2005, 127, 11550–11551. [PubMed: 16104701]

(56). Grapperhaus CA; Mienert B; Bill E; Weyhermüller T; Wieghardt K. Mononuclear (Nitrido)Iron(V) and (Oxo)Iron(IV) Complexes via Photolysis of [(Cyclam-Acetato)FeIII(N3)]+ and Ozonolysis of [(Cyclam-Acetato)FeIIIO3SCF3)]+ Water/Acetone Mixtures. Inorg. Chem 2000, 39, 5306–5317. [PubMed: 11187471]

(57). Pangborn AB; Giardello MA; Grubbs RH; Rosen RK; Timmers FJ. Safe and Convenient Procedure for Solvent Purification. Organometallics 1996, 15, 1518–1520.

(58). Chambers JM; Lindqvist LM; Webb A; Huang DCS; Savage GP; Rizzacasa MA. Synthesis of Biotinylated Episilvestrol: Highly Selective Targeting of the Translation Factors EIF4AI/II. Org. Lett 2013, 15, 1–25. [PubMed: 23286390]

(59). Incarvito C; Lam M; Rhatigan B; Rheingold AL; Qin CJ; Gavrilova AL; Bosnich B. Bimetallic Reactivity. Preparations, Properties and Structures of Complexes Formed by Unsymmetrical Binucleating Ligands Bearing 4- and 6-Coordinate Sites Supported by Alkoxide Bridges. J. Chem. Soc. Dalt. Trans 2001, No. 23, 3478–3488.

(60). Baffert C; Romero I; Jacques P; Deronzier A. Synthesis and Structural Characterization of Five- , Six- , and Seven-Coordinate Mononuclear Manganese (II) Complexes with N - Tridentate Ligands. 2004, 357, 3430–3436.

(61). Mukherjee J; Balamurugan V; Gupta R; Mukherjee R. Synthesis and Properties of Fe III and Co III Complexes : Structures Methyl [2- (2- Pyridyl) Ethyl] (2-Pyridylmethyl) Amine]. Dalton Trans. 2003, 3686–3692.

(62). Petasis DT; Hendrich MP. Quantitative Interpretation of Multifrequency Multimode EPR Spectra of Metal Containing Proteins, Enzymes, and Biomimetic Complexes. Methods Enzymol. 2015, 563, 171–208. [PubMed: 26478486]

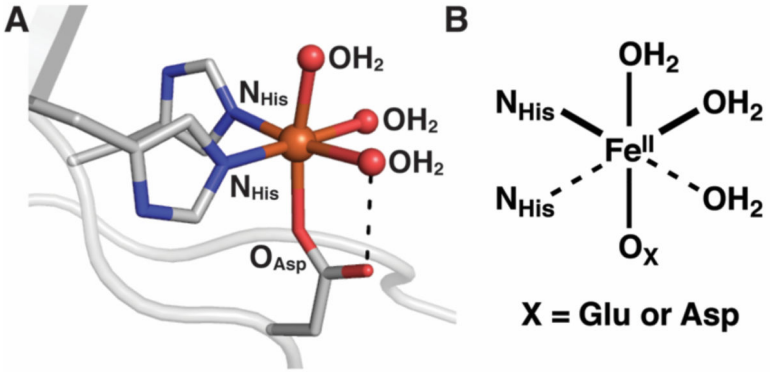

Figure 1.

Fe binding site in cephalosporin synthase showing 2-His-1-carboxylate facial triad (**A**, PDB: 1RXF) and ChemDraw version of the active site (**B**).

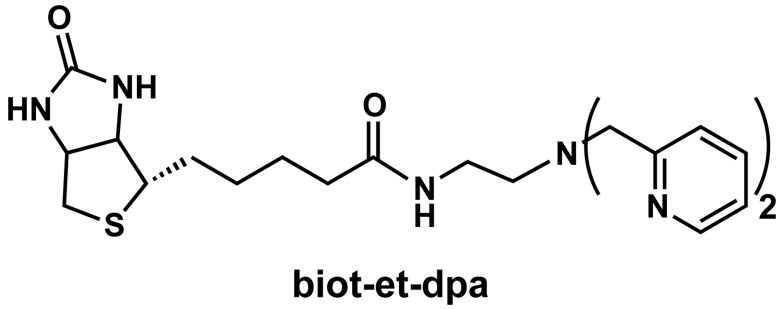

Figure 2.
Biotinylated ligand used in this study.

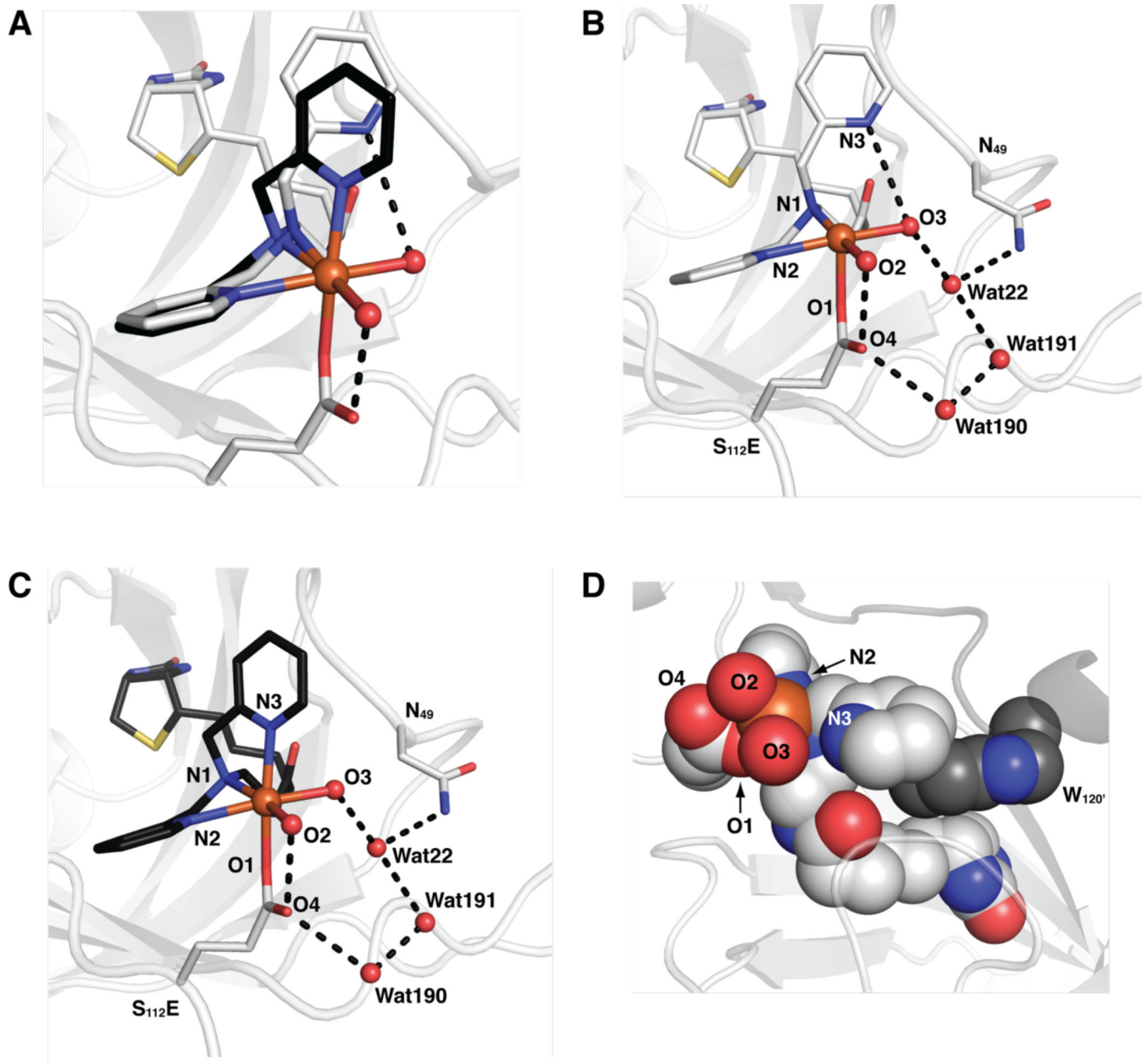

Figure 3.

Overlay of the molecular structures of **1a** (grey) and **1b** (black) (**A**, PDB: 6UIY). The individual molecular structures of **1a** (**B**) and **1b** (**C**) and a partial space-filling representation of **1a** highlighting the π-stacking interaction of the biotinylated Fe^{II} complex that includes one of its pyridine rings with $W_{120'}$ from the neighboring subunit (**D**, dark grey). Fe ions are colored in orange.

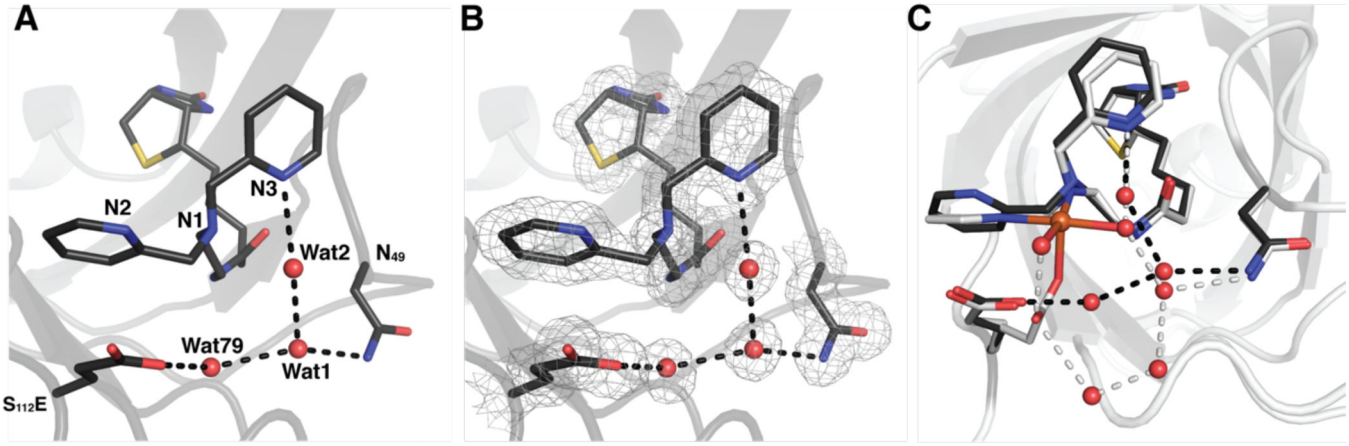

Figure 4.

The molecule structure of biot-et-dpa ⊂ 2xm-S_{112}E-Sav (**A**, PDB: 6UIU). The $2F_0$-F_c electron density map (grey, contoured at 1σ) is highlighted in **B** with same labelling as in **A**. An overlay of biot-et-dpa ⊂ 2xm-S_{112}E-Sav (black) and **1a** (grey) (**C**) that shows the H-bonding networks associated with biot-et-dpa ⊂ 2xm-S_{112}E-Sav (black dashes) and **1a** (grey dashes). The number schemes in **B** & **C** are the same as in **A**.

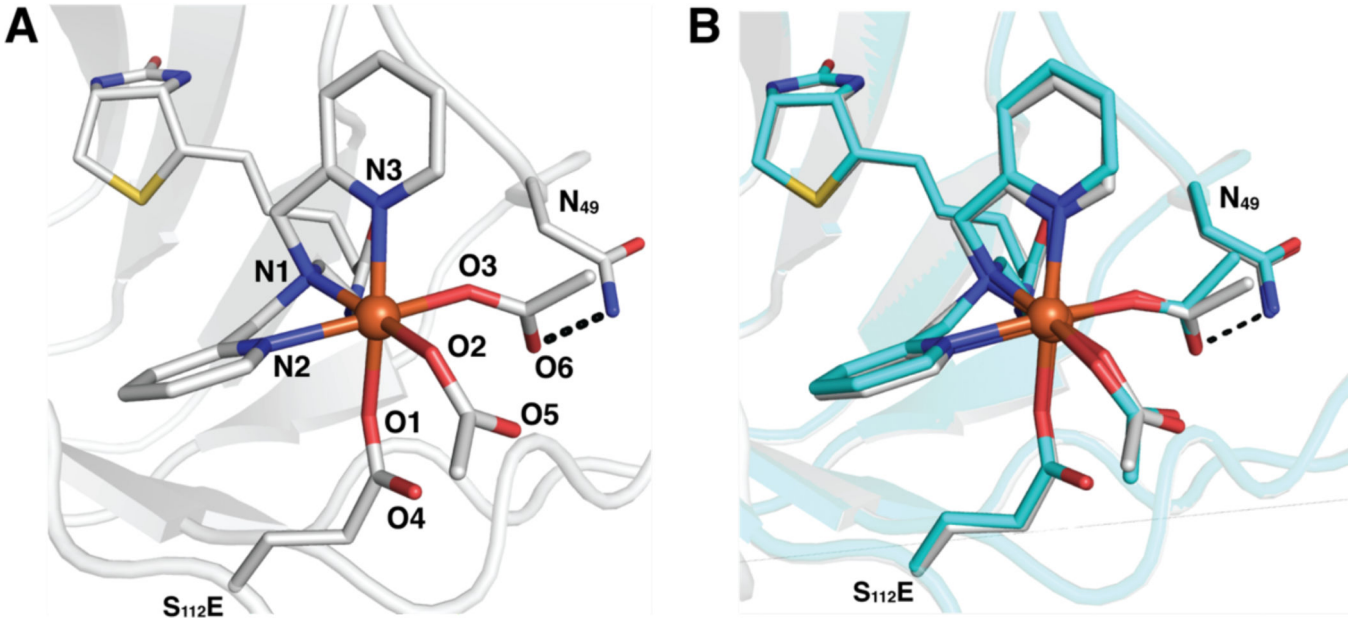

Figure 5.

The molecule structure of **2** (**A**, PDB: 6UIO) and an overlay of the structure collected using XFEL (**B**, carbons colored in teal, PDB: 6US6). The number scheme in **B** is the same as in **A**.

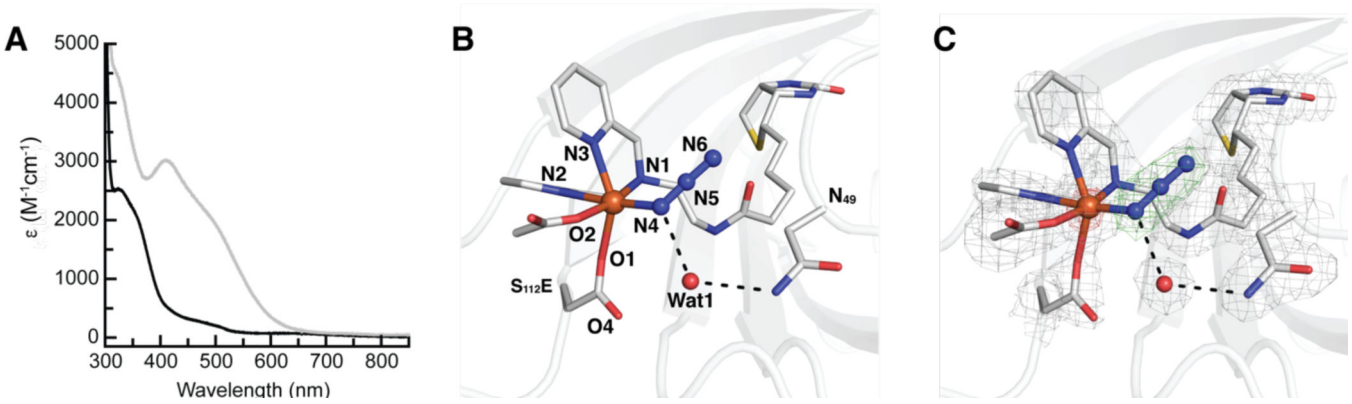

Figure 6.

Electronic absorbance spectra of 2 (black) and **2**–N_3 (grey) recorded at 4°C in 100 mM acetate buffer pH 6 (A). Molecular structure of **2**–N_3 (**B**, PDB: 6UIZ), and the $2F_O$-F_C electron density map (grey, contoured at 1σ), F_O-F_C omit map (green, contoured at 3σ) and anomalous difference density (red, contoured at 5 σ) are shown in C. The numbering scheme in **C** is the same as in **B**.

Table 1.

Selected bond lengths (Å) and angles (˚) for the ArMs from XRD measurements.

Bond lengths and angles	1a	1b	2	2–N_3
Fe–O1	2.16	2.16	2.11	2.35
Fe–O2	2.17	2.17	2.17	2.00
Fe–O3	2.22	2.22	2.15	–
Fe–N1	1.94	2.31	2.15	2.27
Fe–N2	2.32	2.36	2.23	2.52
Fe–N3	–	2.21	2.18	2.27
Fe–N4	–	–	–	2.15
N1–Fe–O2	167	167	167	169
N1–Fe–N2	79	67	71	79
N2–Fe–O3	170	164	165	–
O2–Fe–O3	91	91	96	–
O1–Fe–N1	100	91	90	95
O1–Fe–N2	82	78	79	75
O1–Fe–N3	–	166	164	146
O1–Fe–O2	91	91	96	87
O1–Fe–O3	92	92	95	–
N1–Fe–N3	–	79	76	83
N2–Fe–N3	–	107	104	71
N3–Fe–O2	–	101	100	89
N3–Fe–O3	–	79	78	–
O1–Fe–N4	–	–	–	110
O2–Fe–N4	–	–	–	89
N1–Fe–N4	–	–	–	101
N2–Fe–N4	–	–	–	175
N3–Fe–N4	–	–	–	103
Fe–N4–N5	–	–	–	120

Table 2.

Selected H-bonds (Å) for the ArMs from XRD measurements.

Distances	**1**	**2**	**2–N_3**
N3···O3	3.51	–	–
O3···Wat22	2.54	–	–
Wat22···N49	3.00	–	–
Wat22···Wat191	3.05	–	–
Wat191···Wat190	2.34	–	–
Wat190···O4	3.12	–	–
O4···O2	2.71	–	–
O6···N49	–	2.97	–
N4···Wat1	–	–	2.88
Wat1···N49	–	–	3.17

Table 3.

Comparison of metrical parameters for 1 obtained by XAS and XRD.

Bond	No. of Scatterers	XRD (Å)	XRD (Å)
Average Fe–O/N	5	2.15	2.16
Average Fe···C	4	3.01	3.01
Fe···$C_{methylene}$	1	2.63	2.60